



A Luneburg Lens for the Terahertz Region

Yasith Amarasinghe¹  · Daniel M. Mittleman¹ · Rajind Mendis^{1,2}

Received: 21 August 2019 / Accepted: 14 October 2019 / Published online: 20 November 2019
© Springer Science+Business Media, LLC, part of Springer Nature 2019

Abstract

We experimentally demonstrate a two-dimensional Luneburg lens for the THz region using a waveguide-based artificial-dielectric medium. The substrate material of the lens is Teflon with the top and bottom surfaces coated with silver to form a quasi-parallel-plate waveguide. The top surface of the device has a curved conical profile and the bottom surface is flat. The lens can focus an approximately 2-cm diameter input beam at a frequency of 0.162 THz to a spot size of 3.4 mm (less than 2λ) at the diametrically opposite edge of the device.

Keywords Gradient-index lenses · Artificial dielectrics · Spectroscopy, terahertz · Luneburg lens

A gradient-index (GRIN) lens is an example of an optical device whose focusing effect is realized by a spatial variation of the refractive index of the constituent material [1]. The design and fabrication of devices like GRIN lenses using naturally occurring dielectrics is an ongoing challenge [2]. In particular, it is difficult to realize a continuously varying refractive index, and in some cases, the required high index gradients. Some of the fabrication methods which have been used to approximate a gradient index are the onion-shell technique [3], the tapered-hole approach [4], the slice technique [5], the sub-wavelength microstructuring method [6], and 3D printing methods [7, 8]. Although these approaches can be effective, each suffers from optical aberrations due to the non-ideal, discontinuous index profile. An alternative strategy based on metamaterials [9–12] and artificial dielectrics [13–15] has opened up many possibilities to realize devices with spatially varying dielectric parameters. Of particular interest in the THz range is a waveguide-based artificial-dielectric medium [13]. When a parallel-plate waveguide (PPWG) is excited to operate in its lowest-order transverse-electric (TE_1) mode, it mimics a dielectric medium. By smoothly varying the plate separation, one can achieve a continuously varying index distribution without introducing multi-mode propagation [14, 15]. Here, we exploit this approach to implement one particular GRIN device, a Luneburg lens.

✉ Yasith Amarasinghe
yasith_amarasinghe@brown.edu

¹ School of Engineering, Brown University, Providence, RI, USA

² Present address: Riverside Research, 2640 Hibiscus Way, Beaver Creek, OH, USA

The Luneburg lens, originally proposed in 1944 [16], has been employed as a wide-angle antenna for communications [17, 18] and radar [19, 20] applications. The lens is a spherically symmetric GRIN device that focuses a collimated beam to the diametrically opposite point on the surface, as shown in Fig. 1a. The index distribution of the device is given by [16].

$$n(r) = \sqrt{2 - (r/R)^2}, \quad (1)$$

where R is the radius of the lens and r is the radial distance from the center. Thus, the index varies from a value of 1.414 at the center to a value of 1 at the surface. The unity index at the surface is an added advantage of this type of device, as it eliminates input/output reflection losses due to the impedance matching to free space.

In order to realize an index distribution with values ranging above unity, as is required for a Luneburg lens, the PPWG cannot be filled simply with air, since the effective refractive index of an air-filled PPWG is less than unity [15]. We note that there have been previous attempts [21] to use an air-filled PPWG structure that operated around 30 GHz, using a modified Luneburg lens equation which requires a less-than-unity index in the interior of the device. As a result, the performance of this device was not as an ideal Luneburg lens. In particular, the focusing effect was weak and the focus was displaced from the edge. For higher THz frequencies, these effects would be magnified even further. In addition, the resulting index mismatch at the input and output faces causes energy loss upon input and output coupling. We can overcome all these problems by using a substrate-filled (rather than air-filled) PPWG. In that case, the effective refractive index of the artificial-dielectric medium is given by [13]

$$n = n_s \sqrt{1 - (c/2n_s b f)^2} \quad (2)$$

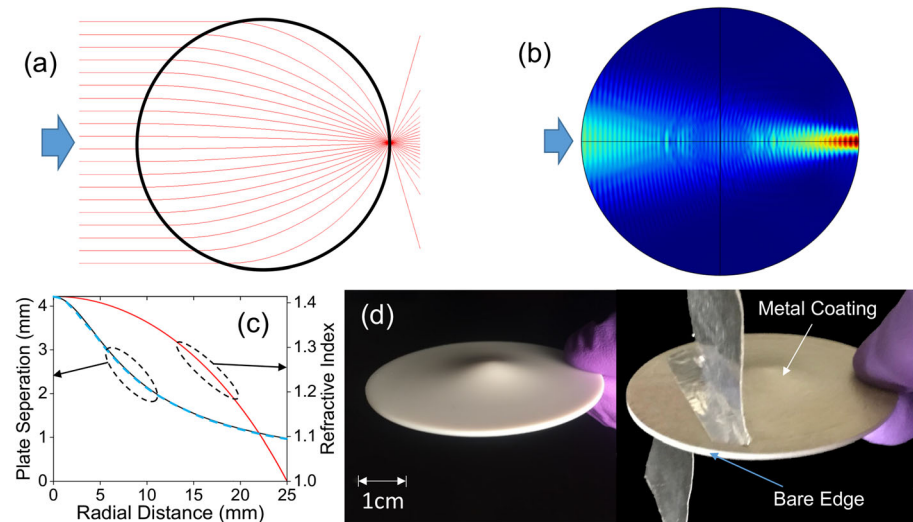


Fig. 1 **a** Ray tracing simulation for a Luneburg lens. **b** FEM simulation showing the electric field distribution for the designed device. **c** The plate separation and the refractive-index profiles of the device. The black solid curve gives the design profile, while the dashed curve gives the measured profile of the fabricated device. **d** Photographs of the machined Teflon substrate before and after the application of silver paint. The after picture also shows the aluminum shields that were used to block any radiation leakage along the top and bottom surfaces

where n_s is the refractive index of the substrate material, b is the plate separation, f is the operating frequency, and c is the vacuum velocity of light. At a chosen frequency (which must be greater than the TE_1 mode cutoff frequency given by $c/(2n_s b)$), we can achieve any value between 0 and n_s for the index simply by adjusting the plate separation b . Therefore, by tailoring the plate separation to vary in two dimensions, in the plane of the PPWG, we can realize an inhomogeneous dielectric medium with a continuously varying effective index. Of course, the variation must be gradual enough so as not to significantly perturb the single-mode propagation in the waveguide. As long as this constraint is satisfied, we can combine Eqs. (1) and (2) to derive an expression for the plate separation which realizes a 2D version of the Luneburg lens:

$$b(r) = \frac{\lambda}{2} \frac{1}{\sqrt{n_s^2 - 2 + (r/R)^2}}, \quad (3)$$

where λ is the vacuum wavelength corresponding to the design frequency.

In comparison, a geodesic lens also uses the height variation of a parallel-plate structure along the radial direction to achieve focusing [22–24]. However, in this case, the mode of interest is the TEM mode of the PPWG. Although the TEM mode is appealing in terms of potential broadband operation, the complicated curvature of the axial profile makes the fabrication quite challenging. In another approach [25], a Luneburg lens was designed using a metallic metasurface in which suitably positioned glide-symmetric holes mimicked the required index profile. In this case, the spatial resolution of the index profile is the size of the unit cell, and again, fabricating these devices for THz frequencies with a smaller cell size would be quite challenging.

The first step in designing the device is to choose the proper substrate material. In order to achieve an index of 1.414 at the center of the lens, we needed a material which has a bulk index greater than this value in the THz regime. At the same time, this material should be transparent to THz radiation, and easily machined, since the device geometry has a non-linear surface profile. We chose ultra-pure Teflon [26] as the substrate material, as it has a relatively frequency-independent index of 1.434 in the vicinity of 0.15 THz, the selected design frequency. In our radially-symmetric prototype device, the radius is chosen to be 2.5 cm. For these design parameters, we can derive the refractive index profile (Eq. (2)) and hence the cross-sectional profile of the device (Eq. (3)). These desired profiles are shown in Fig. 1c (the black and red solid curves). Here, we also plot the measured cross-sectional profile of the fabricated device (blue dashed curve), showing an excellent match to the target design. The height of the device is 0.97 mm at the outer edge and 4.27 mm at the center. Initially, we evaluate the operation of our design using 3D full-wave numerical simulations based on the finite-element method (FEM). A typical result is illustrated in Fig. 1b, showing the electric field distribution of the propagating beam in a plane located 0.5 mm from the bottom (flat) surface of the device. In the simulation, the device is excited by a Gaussian beam with the electric field polarized parallel to the bottom surface, in order to excite the TE_1 mode. We observe a focus at the diametrically opposite edge along the optic axis, as expected. The simulation also shows that there is some irregular propagation in the central region, within 1.5 cm from the center. This is because the plate separation within this region is large enough to support higher-order modes, while the surface curvature is not sufficiently gradual to preserve the single-mode nature of propagation. Despite this issue, the focusing properties of the device are preserved in the simulation, since the device supports only a single mode at the edges, outside of this central region.

We use computer numerical control (CNC) lathe machining to form the Teflon substrate to the required shape with a surface roughness of $25\ \mu\text{m}$. A photograph of the machined device is shown in Fig. 1d, illustrating the curved conical shape of the top surface. The bottom surface is flat. To complete the fabrication of the device, high-conductivity silver paint is applied to both the top and bottom surfaces, leaving the circular (cylindrical) edge bare. These silver coatings act as the metal plates for the dielectric-filled quasi-PPWG.

The experiment is carried out using a fiber-coupled THz time-domain-spectroscopy system. As shown in Fig. 2a, two confocal polythene lenses were used to form a frequency-independent input beam on one facet of the device, and a scanning subsystem that includes two more confocal lenses is used to measure the output beam. The detector subsystem also includes a 1-mm diameter circular aperture to improve the spatial resolution. To excite the TE_1 mode, the polarization of the incident THz beam is aligned parallel to the flat bottom surface of the device. Since the size of the circular input beam is larger than the thickness of the device, we mount aluminum shields on the top and bottom surfaces in close proximity to the input end to block any radiation leakage along the exterior of the two metal surfaces. To measure the output beam, we scan the detector subsystem perpendicular to the optic axis (as indicated by the arrows in Fig. 2) with a step size of 0.5 mm. During this measurement, the minimum gap between the output edge of the device and the aperture was 0.5 mm. For comparison, we also measure the input beam without the device in place, by translating the detector subsystem such that the aperture overlapped with the input plane. For the input beam measurement, we used a larger 1-mm step size.

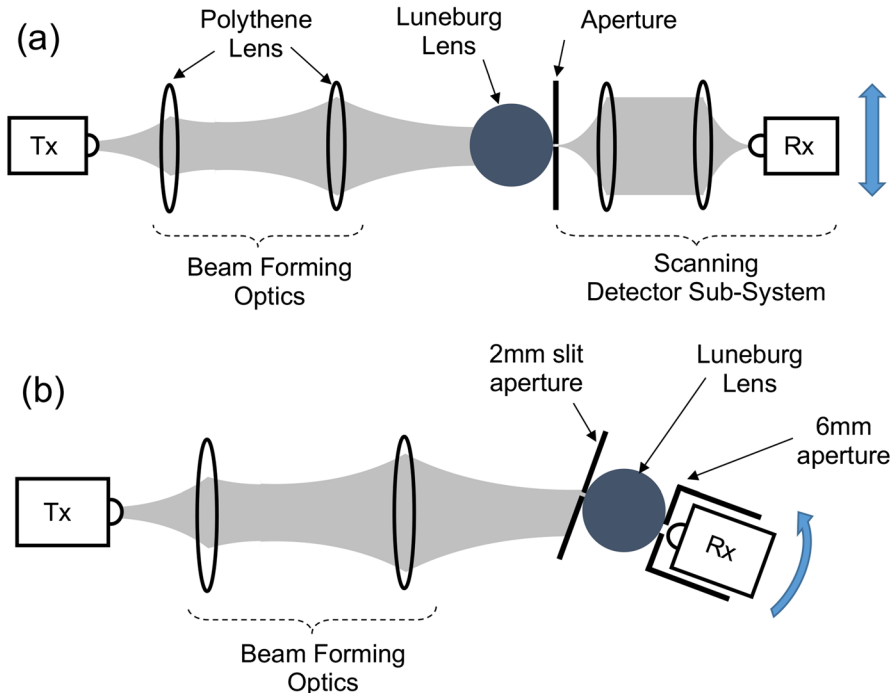


Fig. 2 Schematic diagram of the experimental setup for **a** characterizing the focusing behavior of the lens and **b** demonstrating the beam-steering behavior of the lens. The gray areas represent the propagating THz beam

In analyzing the data, we Fourier transform the detected time-domain signals to extract the spectral amplitude of the electric field at each scanned position. These are then used to construct the electric field profiles of the output and input beams. Figure 3a shows the frequency dependence in the measured $1/e$ -amplitude spot size of the output beam, derived using a Gaussian fit to the measured profile. This indicates a minimum spot size of 3.4 mm, at a frequency of 0.162 THz. This 12-GHz shift from the design frequency is a result of imperfections in the fabricated device. Figure 3b shows the measured electric field profiles of the input and output beams at the frequency of 0.162 THz, in comparison with the FEM simulation results at the same frequency. Both the measurement and simulation results indicate that an 18.6-mm diameter input beam can be focused to a spot size of 3.4 mm. In order to investigate the focusing behavior at other (higher) frequencies, we also measured the output beam profiles at 0.30 THz and 0.45 THz. These have much larger spot sizes of 9.3 mm and 10.8 mm respectively (Fig. 3c). We also observe two peaks in these profiles, most likely due to high-order mode excitation in the device at these higher frequencies.

Beam steering will be an important requirement in directional THz wireless communication systems, in order to enable mobility [27] and to avoid eavesdroppers [28]. A half-Luneburg lens sitting on a mirror surface can be used to steer a beam through an angle of almost 180° in the vertical plane, as shown in the ray optics simulation in Fig. 4a. This configuration also allows beam steering through a full 360° angle in the horizontal plane. This is another unique advantage of the Luneburg lens over a parabolic dish antenna. Beam steering with the dish antenna would require the motion of the whole bulky antenna, whereas with the Luneburg lens, it would require the motion of only the feed point. In order to demonstrate the focusing behavior of a half-Luneburg lens, we investigated two configurations. In one configuration, we used a mirror surface, and in the other, we utilized the phenomenon of total internal reflection (TIR) [4] without using a mirror surface. In the TIR demonstration, we chose an incidence angle of 62° . This is the critical angle for an index of 1.13, which was the effective index of our device at a radius of 2.1 cm. For the demonstration with the mirror surface, we coated the flat

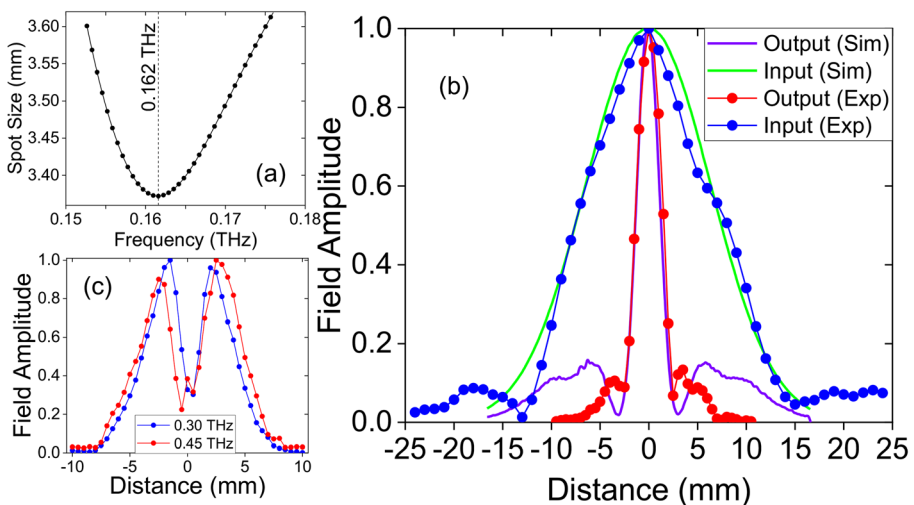


Fig. 3 **a** Measured spot size as a function of the THz frequency. **b** Normalized electric field of the input and output beams at the frequency of 0.162 THz. The closed circles correspond to the measurements and the solid curves correspond to the simulations. **c** Measured electric field of the output beam at 0.30 THz and 0.45 THz

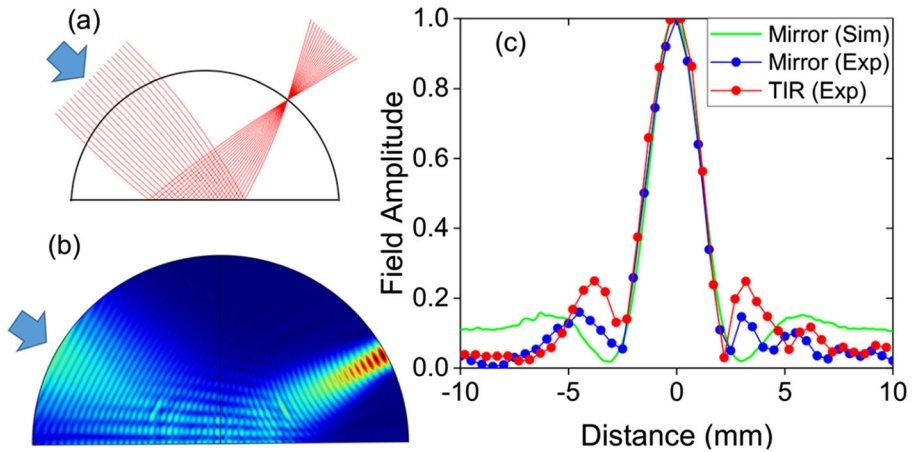


Fig. 4 **a** Ray tracing simulation for a half-Luneburg lens sitting on a horizontal mirror plane. **b** FEM simulation showing the electric field distribution for the designed device, with a mirror plane. **c** Measured electric field of the output at the frequency of 0.162 THz, with and without a mirror plane, compared with the simulation with a mirror plane

(side) surface of the half-Luneburg lens with silver paint. A 3D FEM simulation of this demonstration is shown in Fig. 4b. The measured (normalized) output profiles of these two demonstrations are shown in Fig. 4c, along with the simulation result. From these results, we confirm that the focusing behavior of the fabricated half-Luneburg lens is similar to the behavior of the fabricated full lens, as predicted by ray optics theory (Fig. 4a). In fact, the resulting $1/e$ spot size is also 3.4 mm, equal to that of the full lens. We also observe that the side lobe level is slightly higher in the TIR measurement, most likely caused by the incomplete reflecting (flat-side) surface due to the decreasing index when moving away from the center. As mentioned earlier, and according to (Fig. 1c), the effective index of 1.13 is found at a radius of 2.1 cm. TIR cannot be supported beyond 2.1 cm as the effective index is lower than 1.13.

In the same manner that a Luneburg lens can focus incoming collimated radiation onto a point on its surface, radiation originating from a point source located on its surface can be radiated out of the lens in a collimated beam. As noted above, a unique advantage of this lens geometry is the ability to steer the output beam simply by moving the point source [29, 30]. We demonstrate this steering behavior using our (full) Luneburg lens. In order to simplify the experiment (and to mimic a practical scenario where the feed point is moved), we illuminate the device with a stationary input beam and create a movable point source via the use of a 2-mm slit aperture, as illustrated in Fig. 2b. The 2D FEM simulations shown in Fig. 5a and b correspond to the slit positions of 0° (on axis) and 10° (off axis), respectively, and numerically confirm the expected steering behavior.

To improve the SNR of the detected signal, the bare receiver (with a 6 mm aperture) is located in close proximity to the output edge of the device. Furthermore, in measuring the output beam profile, the receiver is scanned in a circular arc whose center coincides with the geometric center of the device, with a step size of 1° . The input 2-mm slit aperture that defines the point source is scanned along the input edge of the device in 5° steps on both sides of the input axis. At each of these input slit positions, the receiver is scanned azimuthally to characterize the output beam. Figure 5c shows three of the measured output profiles corresponding to the slit positions of -10° , 0° , and $+10^\circ$. Using these measurements, and fitting

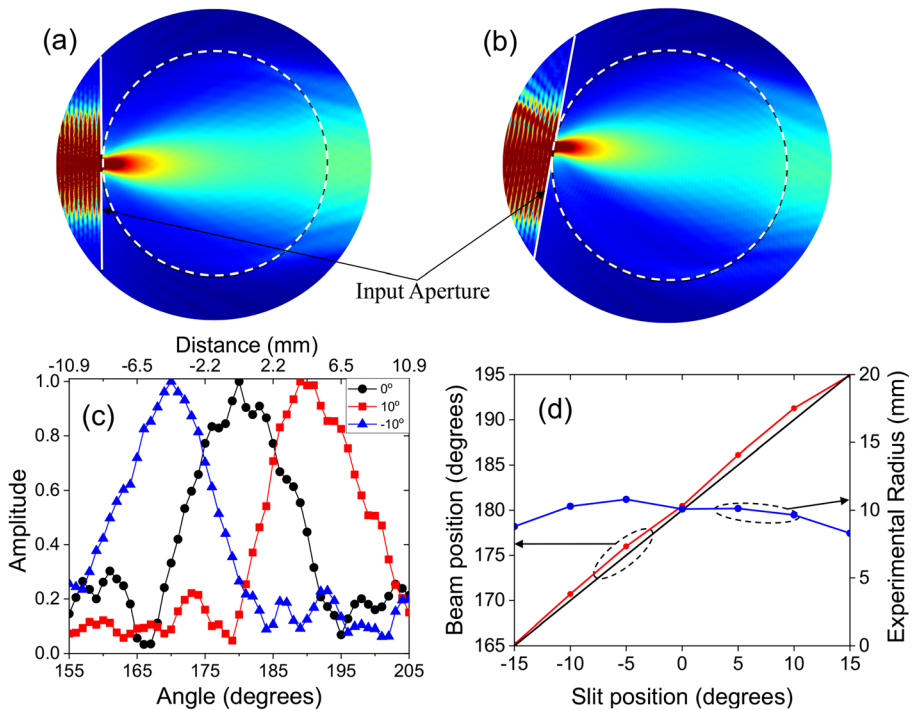


Fig. 5 Beam-steering behavior of the Luneburg lens. 2D FEM simulations showing the electric field distribution when the input slit aperture is **a** on axis and **b** off axis by 10° . The white solid line indicates the input slit aperture. **c** Measured output beam profiles (amplitude vs. angular position of the detector) for input aperture positions of -10° , 0° , and 10° . **d** Estimated position of the output beam and its radius as a function of the input aperture position. The black solid curve gives the theoretical position of the output beam, while the red dotted line gives the experimental position of the output beam

Gaussian profiles, we estimate the output beam position and the beam radius as functions of the input slit position. They exhibit a reasonably linear variation of the output beam's position and a relatively constant beam radius, confirming the expected beam steering of the Luneburg lens. These results are plotted in Fig. 5d. We note that the input slit position and the output beam profile angle are at diametrically opposite ends of the lens. Additionally, the output beam profile angle corresponds to 180° plus the slit position angle.

In conclusion, we implement a 2D Luneburg lens which has an ideal gradient index profile using a waveguide-based artificial-dielectric medium. The lens can focus an 18.6-mm diameter input Gaussian beam at 0.162 THz to a spot size of 3.4 mm at the diametrically opposite point on its edge. We also demonstrate a similar focusing behavior for a half-Luneburg lens with the flat (side) surface uncoated and also with it coated with silver. The silver coating effectively realizes a mirror surface, and the half-lens with the uncoated surface operates via TIR. Furthermore, we also demonstrate the output beam steering of the full lens by characterizing the output beam as a function of the location of a point source at the input side. This prototype device demonstrates the versatility of the waveguide-based artificial-dielectric technology for the realization of exotic GRIN devices for THz applications.

References

1. E. Hecht, *Optics* (Addison-Wesley, 2001).
2. C. Gomez-Reino, M. V. Perez, and C. Bao, *Gradient-Index Optics: Fundamentals and Applications* (Springer, 2010).
3. G. D. M. Peeler and H. P. Coleman, *IRE Trans. Antennas Propag.* **6**(2), 202–207 (1958).
4. K. A. Zimmerman and D. L. Runyon, U.S. Patent No. 5677796 (1997).
5. S. Rondineau, M. Himdi, and J. Sorieux, *IEEE Antennas Wireless Propag Lett.* **2**, 163–166 (2003).
6. M. Brincker, P. Karlsen, E. Skovsen, and T. Søndergaard, *AIP Advances* **6**(2), 025015 (2016).
7. A. I. Hernandez-Serrano, M. Weidenbach, S. F. Busch, M. Koch, and E. Castro-Camus, *Journal of the Optical Society of America B* **33**(5), 928–931 (2016).
8. S. Biswas, A. Lu, Z. Larimore, P. Parsons, A. Good, N. Hudak, B. Garrett, J. Suarez and M. S. Mirotznik, *Microwave and Optical Technology Letters* **61**(4), 1022–1029 (2019).
9. R. A. Shelby, D. R. Smith, S. C. Nemat-Nasser, and S. Schultz, *Appl. Phys. Lett.* **78**(4), 489–491 (2001).
10. D. R. Smith, J. B. Pendry, and M. C. K. Wiltshire, *Science* **305**(5685), 788–792 (2004).
11. N. Kundtz and D. R. Smith, *Nature Materials* **9**, 129–132 (2010).
12. J. Valentine, S. Zhang, T. Zentgraf, E. Ulin-Avila, D. A. Genov, G. Bartal, and X. Zhang, *Nature* **455**, 376–379 (2008).
13. R. Mendis and D. M. Mittleman, *IEEE Trans. Microw. Theory Tech.* **58**(7), 1993–1998 (2010).
14. R. Mendis, J. Liu, and D. M. Mittleman, *Appl. Phys. Lett.* **101**(11), 111108 (2012).
15. J. Liu, R. Mendis, and D. M. Mittleman, *Appl. Phys. Lett.* **103**(3), 031104 (2013).
16. R. Luneburg, *Mathematical Theory of Optics* (Brown University, 1944).
17. P. Afanasyev, S. Matitsine, V. Sledkov, P. Lagoiski, L. Matytsine, and T. DeMarco, *IEEE European Conference on Antennas and Propagation* (2015).
18. A. Demetriadou and Y. Hao, *Opt. Express* **19**(21), 19925–19934 (2011).
19. L. Xue and V.F. Fusco, *IET Microwaves Antennas & Propagation* **1**(3), 624–628 (2007).
20. C. S. Liang, D. A. Streater, J. Jin, E. Dunn, and T. Rozendal, *Antennas Propag. Mag.* **47**(2), 30–42 (2005).
21. C. Hua, X. Wu, N. Yang and W. Wu, *IEEE Trans. Microwave Theory Tech.* **61**(1), 436–443 (2013).
22. K.S. Kunz, *J. Appl. Phys.* **25**(5), 642–653 (1954).
23. R. C. Mitchell-Thomas, O. Quevedo-Teruel, T. M. McManus, S. A. R. Horsley, and Y. Hao, *Opt. Lett.* **39**(12), 3551–3554 (2014).
24. Q. Liao, N. J. G. Fonseca, and O. Quevedo-Teruel, *IEEE Trans. Antennas Propag.* **66**(12), 7383–7388 (2018).
25. O. Quevedo-Teruel, J. Miao, M. Mattsson, and A. A. Brazalez, *IEEE Trans. Antennas Propag.* **17**(9), 1588–1592 (2018).
26. S. Wietzke, C. Jansen, M. Reuter, T. Jung, D. Kraft, S. Chatterjee, B.M. Fischer, and M. Koch, *J. Molec. Struct.* **1006**(1–3), 41–51 (2011).
27. B. Zhou, Y. Yang, H. Li, and T. J. Cui, *J. Appl. Phys.* **110**(8), 084908 (2011).
28. J. Ma, R. Shrestha, J. Adelberg, C. Yeh, Z. Hossain, E. Knightly, J. Miquel Jomet and D. Mittleman, *Nature* **563**, 89–93 (2018).
29. Y. Li, M. Liang, X. Yu, Q. Zhu, H. Xin, *Proc. IEEE Antennas Propag. Soc. Int. Symp. (APSURSI)*, pp. 1274–1275 (2014).
30. M. Liang, X. Yu, R. Sabory-García, W. Ng, M. E. Gehm, and H. Xin, *IEEE MTT-S International Microwave Symposium* (2013).

Publisher's Note Springer Nature remains neutral with regard to jurisdictional claims in published maps and institutional affiliations.